**Wind and Structures**, *Vol. 19, No. 6 (2014) 649-663*
DOI: http://dx.doi.org/10.12989/was.2014.19.6.649 

# Unsteady aerodynamic forces on a vibrating long-span curved roof

Wei Ding[*1], Yasushi Uematsu[2a], Mana Nakamura[3] and Satoshi Tanaka[4]

[1]*School of Mechanics and Civil Engineering, China University of Mining and Technology, Xuzhou, China*
[2]*Department of Architectural and Building Science, Tohoku University, Sendai, Japan*
[3]*Nikken Steel and Sumitomo Metal Corporation, Tokyo, Japan*
[4]*Nikken Sekkei Ltd., Tokyo, Japan*

*(Received April 29, 2014, Revised October 13, 2014, Accepted November 6, 2014)*

**Abstract.** The present paper discusses the characteristics of unsteady aerodynamic forces on long-span curved roofs. A forced vibration test is carried out in a wind tunnel to investigate the effects of wind speed, vibration amplitude, reduced frequency of vibration and rise/span ratio of the roof on the unsteady aerodynamic forces. Because the range of parameters tested in the wind tunnel experiment is limited, a CFD simulation is also made for evaluating the characteristics of unsteady aerodynamic forces on the vibrating roof over a wider range of parameters. Special attention is paid to the effect of reduced frequency of vibration. Based on the results of the wind tunnel experiment and CFD simulation, the influence of the unsteady aerodynamic forces on the dynamic response of a full-scale long-span curved roof is investigated on the basis of the spectral analysis.

**Keywords:** unsteady aerodynamic force; long-span curved roof; wind tunnel experiment; CFD simulation; dynamic response

## 1. Introduction

Wind-structure interaction is a critical consideration in the design of many structures in civil engineering, especially for the structure being flexible and light, such as the long-span bridges, high-rise buildings and long-span roofs. Such structures are generally vulnerable to dynamic wind actions. The wind-structure interaction is represented by the unsteady (or motion-induced) aerodynamic force, which may affect the wind-induced response, significantly. Many researches have been made of the unsteady aerodynamic forces on long-span bridges and high-rise buildings (e.g., Matsumoto *et al.* 1996, Sato *et al*. 2000, Matsumoto *et al*. 2010, Cooper *et al.* 1997, Cheng *et al*. 2002, Chen 2013). The results indicate that unstable vibrations may be induced by the negative aerodynamic damping in some cases. By comparison, the number of researches on long-span roofs is quite limited. Ohkuma *et al.* (1990) investigated the mechanism of aeroelastic instability for long-span flat roofs using a forced vibration test in a wind tunnel. Daw and Davenport (1989) carried out a forced vibration test on a semi-circular roof to investigate the

*Corresponding author, Ph. D., E-mail: tei.ding.wei@gmail.com
[a] Professor, E-mail: yu@archi.tohoku.ac.jp


http://www.techno-press.org/?journal=was&subpage=8 ISSN: 1226-6116 (Print), 1598-6225 (Online)

dependence of unsteady aerodynamic forces on the turbulence intensity, wind speed, vibration amplitude and geometric details of the roof. Uematsu (1982) conducted a series of wind tunnel tests using elastic models of a one-way type of suspended roof. The growth mechanism of the wind-induced vibrations and the effect of wind-roof interaction on the dynamic response were discussed. Yang *et al*. (2010) investigated the interaction between wind and membrane structures using the wind tunnel experiment. They found that the effect of dynamic interaction is significant in the wind-induced response and the structural natural frequency is decreased due to the wind-structure interaction. At present, however, the characteristics of unsteady aerodynamic forces on long-span curved (vaulted) roofs are not understood well. Therefore, it is necessary to investigate this problem further for proposing more reasonable methods of response analysis for these roofs.

The objective of the present study is to describe the characteristics of unsteady aerodynamic forces acting on a long-span curved roof vibrating in the first anti-symmetric mode. First, a forced-vibration test is carried out in a wind tunnel. The effects of wind speed, vibration amplitude and frequency on the characteristics of unsteady aerodynamic forces are investigated. However, the range of these parameters involved in the wind tunnel experiment is limited. Therefore, a CFD simulation is carried out to investigate the problem in more detail. In the simulation, the reduced frequency of vibration is varied over a wider range. Finally, a discussion is made of the dynamic response of a full-scale long-span curved roof with consideration of the effect of unsteady aerodynamic forces.

## 2. Description of unsteady aerodynamic force

The displacement of the roof in the *j*-th mode may be represented by the following equation

$$z_j(s,t) = \phi_j(s) x_j(t) \tag{1}$$

where $\phi_j$ and $x_j$ are the mode shape and generalized displacement of the *j*-th mode, respectively; and *s* represents the circumferential coordinate taken along the roof.

Applying a modal analysis to the equation of motion for the roof, we obtain the following equation of motion for the *j*-th generalized displacement

$$\ddot{x}_j(t) + 2\zeta_j \omega_j \dot{x}(t) + \omega_j^2 x_j(t) = F_j(t) / M_j \tag{2}$$

$$F_j(t) = F_{W_j}(t) + F_{A_j}(x_j, \dot{x}_j, \ddot{x}, ...) \tag{3}$$

where $M_j$= generalized mass;$\omega_j$= natural circular frequency; $\zeta_j$= critical damping ratio; and $F_j$= generalized force. $F_{Wj}$ represents the fluctuating wind force due to the oncoming flow and wake instability, while $F_{Aj}$ the unsteady aerodynamic force due to the wind-roof interaction.

In the case of forced-vibration test, a steady vibration in the first anti-symmetric mode represented by a sine curve is applied to the roof. The unsteady aerodynamic force $F_{Aj}$ (here $j$ = 1) may be obtained from Eq. (4) by using the Fourier series at the frequency $f_m$ of the forced vibration

$$F_{A_j}(t) = F_{R_j} \cos 2\pi f_m t - F_{I_j} \sin 2\pi f_m t \tag{4}$$

where $F_{Rj}$ and $F_{Ij}$are the in-phase and out-of-phase components of the unsteady aerodynamic force, respectively.

The effect of unsteady aerodynamic force may be evaluated by the aerodynamic stiffness and damping coefficients $a_{Kj}$ and $a_{Cj}$, which are given by the Eqs. (5) and (6).

$$a_{K_j} = \frac{F_{R_j}}{q_H A_s (x_0 / L)} = \frac{1}{q_H A_s (x_0 / L)} \frac{2}{T} \int_0^T F_j(t) \cos 2\pi f_m t dt \tag{5}$$

$$a_{C_j} = \frac{F_{R_j}}{q_H A_s (x_0 / L)} = \frac{1}{q_H A_s (x_0 / L)} \frac{2}{T} \int_0^T F_j(t) \sin 2\pi f_m t dt \tag{6}$$

where $q_H$ = velocity pressure at the mean roof height $H$; $A_s$ = roof area; $x_0$ = forced vibration amplitude; $L$ = span of the roof; $f_m^*$ = reduced frequency of vibration, defined by $f_m H/U_H$, with $U_H$ being the mean wind speed at the mean roof height $H$.

## 3. Wind tunnel experiment

In order to investigate the characteristics of unsteady aerodynamic forces, a forced vibration test is conducted in a wind tunnel. The influences of wind speed, vibration amplitude, reduced frequency of vibration and rise/span ratio of the roof on the unsteady aerodynamic forces are investigated.

### *3.1 Experimental arrangement and procedure*

The experiments were carried out in an Eiffel-type wind tunnel with a working section 6.5 m in length and 1.0 m×1.4 m in cross-section. A turbulent boundary layer with a power-law exponent of $\alpha$=0.23 was generated on the wind tunnel floor by using a set of turbulence-generating spires installed at the entrance of the working section, and a number of roughness blocks distributed on the floor. The profiles of the mean wind speed and turbulence intensity are shown in Fig. 1. The reference wind speed was measured at a height of $Z_G$ = 500 mm. The longitudinal velocity spectrum, not shown here to save space, was found to be generally consistent with the so-called Karman type spectrum.

The wind tunnel model was a curved roof made of 0.8 mm thick polyester film, as shown in Figs. 2 and 3. Two models with rise/span ratios of 0.15 and 0.20 were tested. The forced-vibration equipment used in the experiment is shown in Fig. 4. A pair of end plates was set on the edge of model to make the flow two dimensional. Each model had 12 pressure taps of 1mm diameter distributed along the roof's centerline. The pressure taps were connected to pressure transducers in parallel via 80 cm lengths of flexible vinyl tubing. The tubing effects were numerically compensated by using the gain and phase-shift characteristics of the pressure measuring system used in the experiment. The signals from the pressure transducers were sampled simultaneously at a rate of 500 Hz for a period of approximately 60s. Table 1 summarizes the range of experimental parameters involved in the wind tunnel experiment.

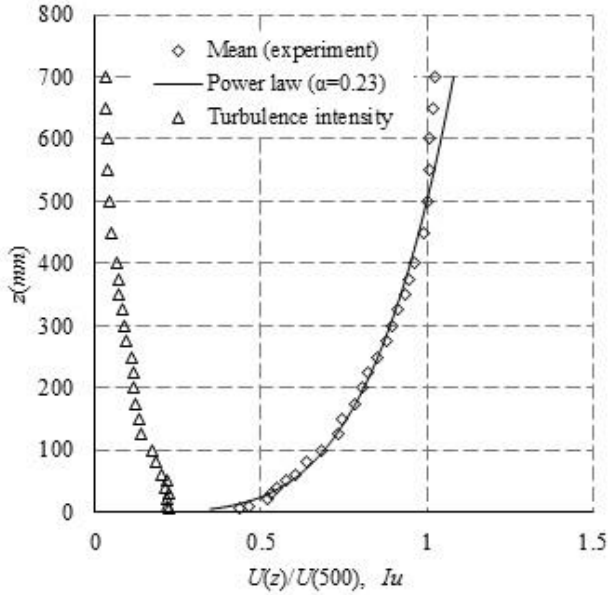


Fig. 1 Profiles of the mean wind speed and turbulence intensity

Fig. 2 Photo of experimental model

$L$ =400mm
$D$ =240mm
$H$ =80mm ($r/L$=0.15)
$H$ =90mm ($r/L$=0.20)
$r$ =60mm ($r/L$=0.15)
$r$ =80mm ($r/L$=0.20)
$h$ =50mm

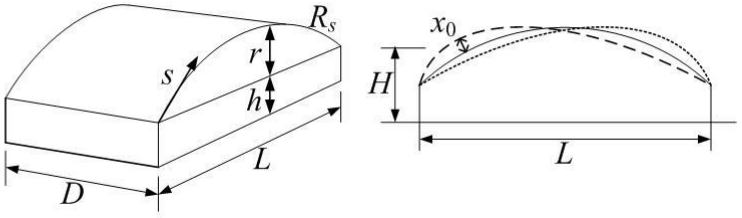


Fig. 3 Geometry of the experimental model

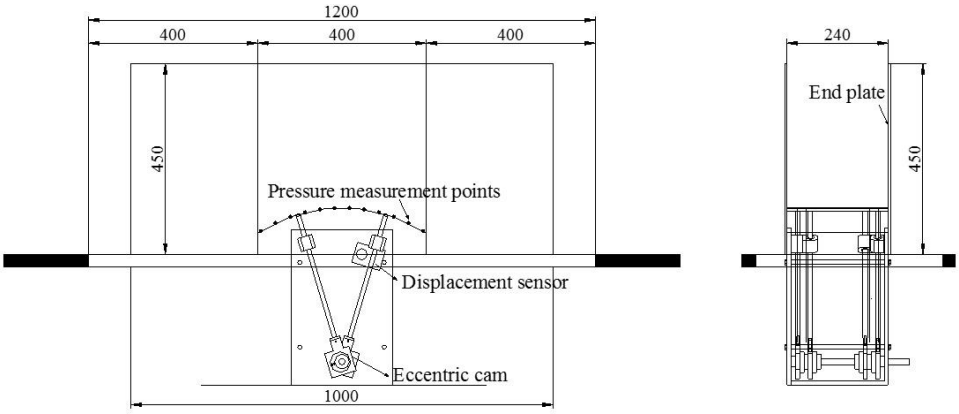


Fig. 4 Experimental setup of the forced vibration test

Table 1 Parameters of experiment

| | |
|---|---|
| Rise/span ratio $r/L$ | 0.15, 0.20 |
| Wind speed $U_H$ (m/s) | 5.0, 7.0, 10.0 |
| Amplitude of the forced vibration $x_0$ (mm) | 1.0, 2.5, 4.0 |
| Forced vibration frequency $f_m$ (Hz) | 5 to 25 at an increment of 1 Hz |

### *3.2 Results and discussion*

Fig. 5(a) and 5(b) shows the variation of the aerodynamic stiffness coefficient $a_K$ with the reduced frequency of vibration $f_m^*$ (= $f_m H/U_H$) for various wind speeds and vibration amplitudes; the rise/span ratio $r/L$ is 0.15. The value of $a_K$ generally increases with an increase in $f_m^*$. As the reduced frequency of vibration decreases, the value of $a_K$ approaches the quasi-steady value (dashed line in the figure). Similar results were observed for $r/L$ =0.20. Within the limits of the present experiment, the value of $a_K$ is generally positive, which may reduce the total stiffness of the structural system, resulting in a lower natural frequency.

Plotted on Figs. 6(a) and 6(b) is the variation of aerodynamic damping coefficient $a_C$ with $f_m^*$ for various wind speeds and vibration amplitudes. The values of $a_C$ are generally negative except for small $f_m^*$values, which may increase the total damping of the structural system. The magnitude of $a_C$ increases as the $f_m^*$ value increases. Similar results were observed for $r/L$ =0.20. It can be seen that the effects of wind speed and vibration amplitude on the aerodynamic stiffness and damping coefficients are relatively small and the values of $a_K$ and $a_C$ are mainly dependent on $f_m^*$.

## 4. CFD simulation

Because the range of wind tunnel experiment is limited, a CFD simulation is carried out to reproduce the wind tunnel experiment and investigate the characteristics of unsteady aerodynamic forces in a wider range of reduced frequency of vibration.

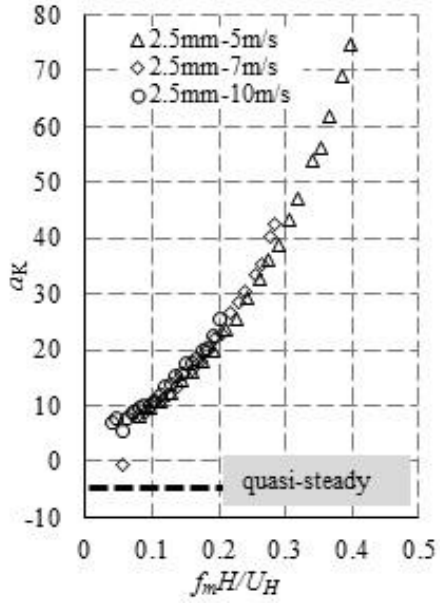


(a) Wind speed

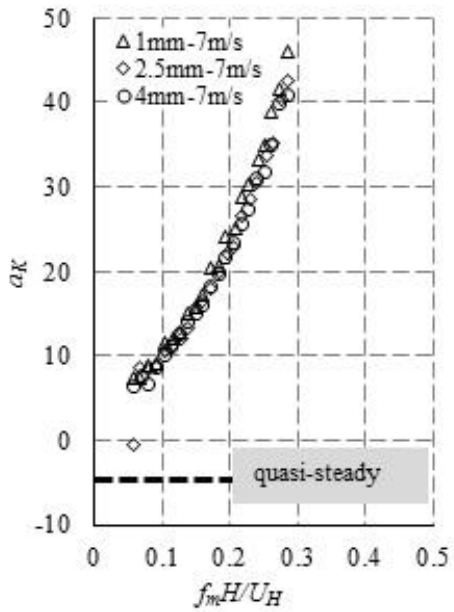


(b) Vibration amplitude

Fig. 5 Aerodynamic stiffness coefficient versus $f_m^*$ ($r/L$=0.15)

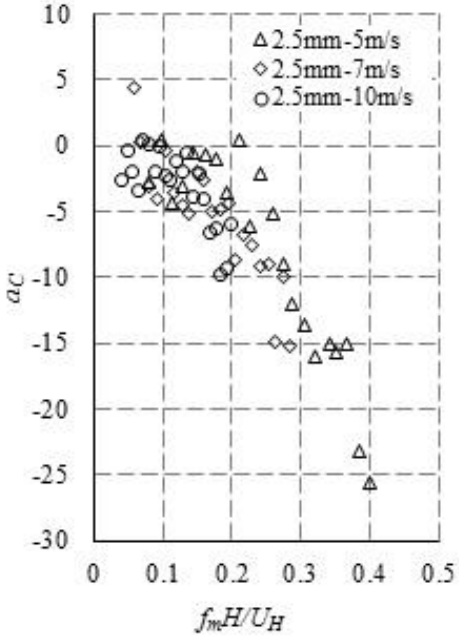


(a) Wind speed

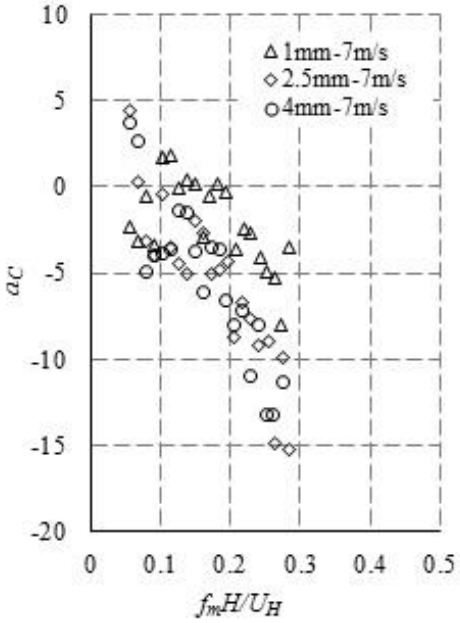


(b) Vibration amplitude

Fig. 6 Aerodynamic damping coefficient versus $f_m^*$ ($r/L$=0.15)

### *4.1 Computational conditions*

The simulation is carried out by using a CFD software 'STAR-CD', in which LES with the Smagorinsky sub-grid model ($C_s$=0.12) is used (Sarwar *et al*. 2008, Ono *et al*. 2008, Lu *et al*. 2012). The computational domain is shown in Fig. 7(a). In the simulation, we calculated various types of mesh arrangements. The results were compared with those of wind tunnel experiment. And then the mesh arrangement was selected which leads to the most corresponding results with that of experiment, as shown in Fig. 7(b). Two-dimensional flow is simulated similar to that used in the wind tunnel experiment. The model is forced to vibrate in the first anti-symmetric mode by using dynamic mesh technique. Table 2 summaries the parameters investigated in the CFD simulation. The rise/span ratio of model is 0.15. The amplitude of vibration $x_0$ is fixed to 4.0 mm. We discuss the effect of unsteady aerodynamic forces in a wider range of reduced frequency of vibration, changing the forced-vibration frequency from 0 to 160 Hz. The range of reduced frequency $f_m^*$ of vibration is from 0 to 2.5, which satisfies the principle of similarity to practical long-span curved roofs.

The computational and boundary conditions are summarized in Table 3. The inflow turbulence is generated in a preliminary computational domain. The governing equations are discretized based on the finite volume method.

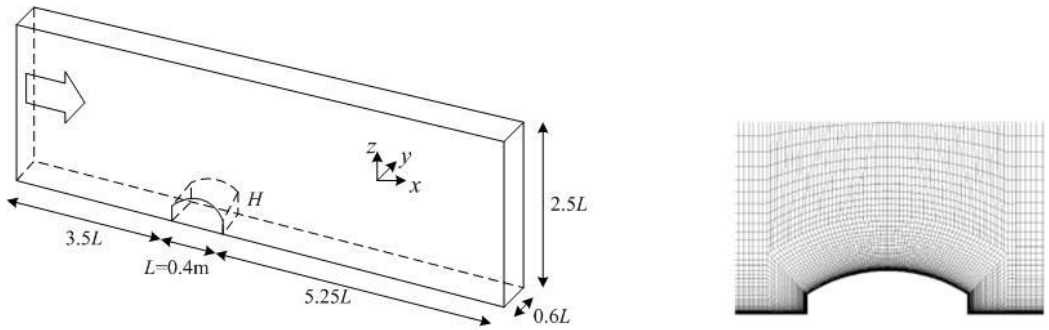


(a) Computational domain (b) Mesh arrangement

Fig. 7 Computational domain and mesh arrangement

Table 2 Computational parameters

| | |
|---|---|
| Rise/span ratio $r/L$ | 0.15 |
| Wind speed $U_H$ (m/s) | 5.0 |
| Amplitude of the forced vibration $x_0$( mm) | 4.0 |
| Forced vibration frequency $f_m$ (Hz) | 0~ 160Hz (@ 10 Hz) |
| Reduced frequency of vibration $f_m^*$ | 0 ~ 2.5 |

Table 3 Computational and boundary conditions

| | |
|---|---|
| Computational domain | $9.75L(x)\times0.6L(y)\times2.5L(z)$ |
| Inlet boundary | Inflow turbulence is generated in preliminary computational domain |
| Upper boundary | Zero normal velocity and zero normal gradients of other variables |
| Side boundary | Cyclic boundary conditions |
| Outlet boundary | Zero normal gradients of all variables |
| Floor and model surfaces | no-slip condition |
| Grid discretization | $260(x) \times 24(y) \times 64(z)$= (199,680) |
| Convection schemes | Centered difference scheme |
| Time differential schemes | Euler Implicit |
| Numerical algorithm | PISO algorithm |
| Time step | $\Delta t$ = 2.0E-04 second (Courant Number：9.1E-02) |

A preliminary LES is used to generate the inflow turbulence and store the time history of velocity fluctuations (Nozu and Tamura 1998). Fig. 8 shows the domain of the preliminary computation. The roughness blocks with heights of 3, 5 and 8 cm are arranged on the ground of preliminary computational domain. The periodic boundary condition is used at the inlet and outlet boundaries. Furthermore, the pressure gradient ($\Delta p$) is applied to the inlet boundary. The profiles of the mean wind speed and turbulence intensity at the inlet of the main computational domain are compared with those of the wind tunnel flow as shown in Fig. 9. It can be seen that the inflow turbulence used in the LES is generally in good agreement with that used in the wind tunnel experiment.

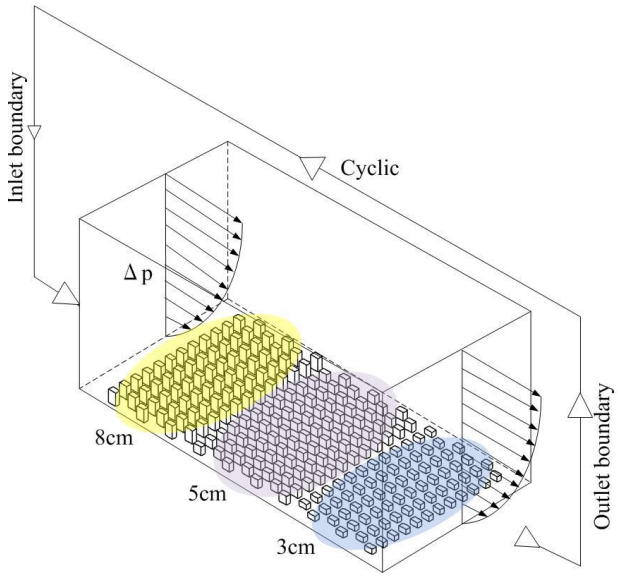


Fig. 8 Preliminary computational domain

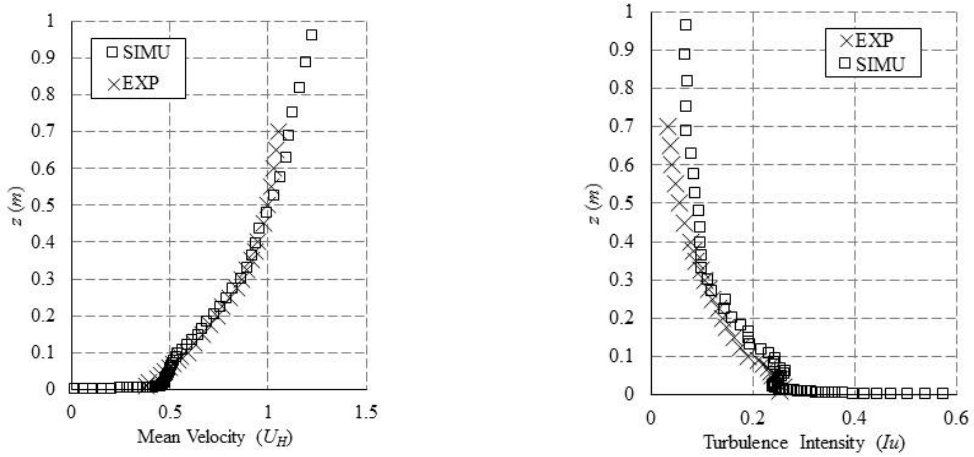


(a) Mean velocity (b) Turbulence intensity

Fig. 9 Comparison of mean velocity and turbulence intensity of turbulent boundary layer between CFD simulation and wind tunnel experiment

### *4.2 Computational results*

In order to validate the accuracy of the CFD, the distribution of the mean wind pressure coefficient along the centerline of the vibrating roof is compared with that obtained from the wind tunnel experiment. Fig. 10 shows the results, in which the results for the frequencies of 0, 10 and 15Hz are plotted. A generally good agreement between these two results can be seen. The difference is somewhat larger near the top and leeward of roof; the variance is approximately 10% between CFD values and experimental values. This difference may be due to a difference in surface roughness of the roof between CFD simulation and wind tunnel experiment. Besides, the wind pressure tap used in the wind tunnel experiments could also cause the variance.

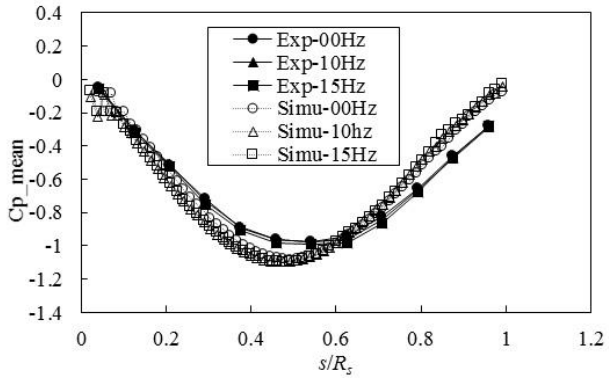


Fig. 10 Comparisons between CFD simulation and wind tunnel experiment for the mean wind pressure coefficient

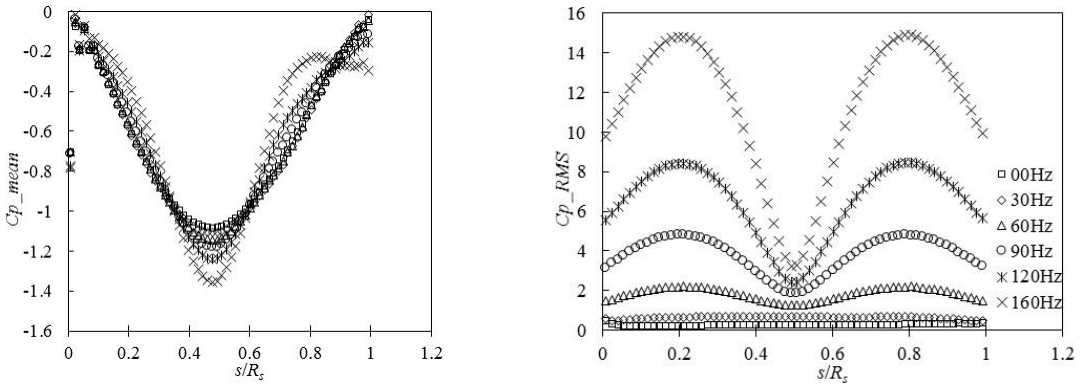


(a) Mean wind pressure coefficients (b) RMS wind pressure coefficients

Fig. 11 Variation of mean and RMS wind pressure coefficients with forced vibration frequency

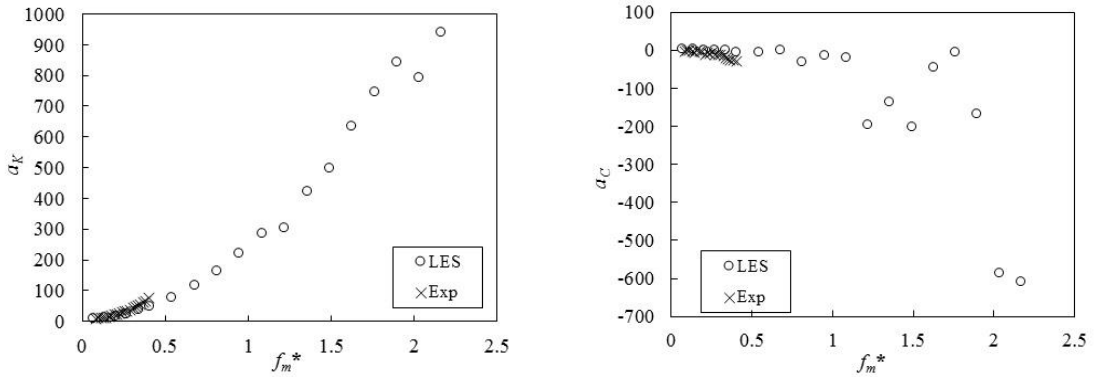


(a) Aerodynamic stiffness coefficients (b) Aerodynamic damping coefficients

Fig. 12 Aerodynamic stiffness and damping coefficients versus $f_m^*$

The distributions of mean and RMS fluctuating wind pressure coefficients for various forced-vibration frequencies are shown in Fig. 11. It can be seen that the mean wind pressure coefficients near the rooftop increase in magnitude and the RMS fluctuating wind pressure coefficients generally increase, as the forced-vibration frequency increases. Furthermore, the variation is significant near the position of the largest forced-vibration amplitude. The results indicate that the wind pressure field around the vibrating roof is significantly influenced by the vibration itself.

Based on the results of CFD simulation, the aerodynamic stiffness and damping coefficients are calculated by using Eqs. (5) and (6). Fig. 12 shows the aerodynamic stiffness and damping coefficients, $a_K$ and $a_C$, obtained from the CFD simulation and wind tunnel experiment, as a function of the reduced frequency $f_m^*$ of vibration. The wind tunnel experiment was carried out in a limited range of $f_m^*$, while the CFD simulation was made over a wider range of $f_m^*$. It can be seen the variation of $a_K$ and $a_C$ with $f_m^*$ shows the same tendency with that obtained from the wind tunnel experiment; the magnitude of $a_K$ and $a_C$ increases with an increase in $f_m^*$.

## 5. Prediction of dynamic response

Based on the results of the aerodynamic stiffness and damping coefficients $a_K$ and $a_C$ obtained from the wind tunnel experiment and CFD simulation, we evaluate the effect of the unsteady aerodynamic forces on the dynamic response of a full-scale long-span curved roof by using the spectral analysis.

### *5.1 Theoretical analysis of response*

As an example, we consider a full-scale long-span membrane structure with the same shape as that used in the wind tunnel experiment. In general, the natural frequency of membrane structure with a span of approximately 100 m is in a range from 0.5 to 1.5 Hz and the mass from 2 to 15 kg/m$^2$. The dynamic responses of such structures in a turbulent flow are evaluated based on the aerodynamic stiffness and damping coefficients obtained from the wind tunnel experiments and CFD simulation.

Aerodynamic stiffness ($K_{aj}$) and aerodynamic damping ratio ($\zeta_{aj}$) are estimated from the aerodynamic stiffness and damping coefficients by using Eqs. (7) and (8) (Katagiri *et al.* 2001). The mechanical admittance $H_j(f)$ including the aerodynamic stiffness and damping is defined by Eq. (9) and the standard deviation of generalized displacement $\sigma_{xj}$ is derived from Eq. (10), in which we assume that the structural damping ratio is $\zeta_s$ = 3 % and the natural frequency of the first anti-symmetric mode is $f_s$ = 0.5 Hz. In Eq. (10), the modal force spectrum $S_{Fj}(f)$ is taken from the experimental results. Only the first vibration mode ($j$=1) is considered, because the roof response to turbulent wind forces is thought to be dominated by this mode (Katagiri *et al.* 2001).

$$\frac{K_{a_j}(f)}{K_{s_j}} = -\frac{1}{8\pi^2}\frac{\rho_a}{\rho_{s_j}}\left(\frac{U_H}{f_{s_j}H}\right)^2\frac{H}{L}a_{K_j}(f) \tag{7}$$

$$\zeta_{a_j}(f) = -\frac{1}{16\pi^2}\frac{\rho_a}{\rho_{s_j}}\left(\frac{U_H}{f_{s_j}H}\right)^2\frac{H}{L}a_{C_j}(f) \tag{8}$$

$$\left|H_j(f)\right|^2 = \frac{1}{\left[1-\left(\frac{f}{f_{s_j}}\right)^2+\frac{K_{a_j}(f)}{K_{s_j}}\right]^2+4(\zeta_{s_j}+\zeta_{a_j}(f))^2\left(\frac{f}{f_{s_j}}\right)^2} \tag{9}$$

$$\sigma_{x_j}^2 = \frac{1}{K_{0_j}^2}\int_0^\infty S_{F_j}(f)\left|H_j(f)\right|^2 df \tag{10}$$

### *5.2 Results of dynamic responses*

Fig. 13 illustrates the mechanical admittance functions plotted against the frequency $f$ for various wind speeds, where the mass per unit area of the roof is assumed $M_s$ = 4 kg/m$^2$. As the wind speed increases, the resonant frequency decreases and the peak value of the mechanical admittance function at the resonant frequency increases. This feature may be due to the effect of

positive aerodynamic stiffness coefficient.

The effect of the mass $M_s$ on the mechanical admittance function is illustrated in Fig. 14, in which we assume that $U_H$ = 20 m/s. The resonant frequency increases and the resonant peak value of the mechanical admittance function decreases as the roof's mass increases. This feature implies that the increase in mass is quite effective for reducing the wind excitation of the roof. In other words, the effect of unsteady aerodynamic forces on the response of the roof becomes less significant for heavier roofs.

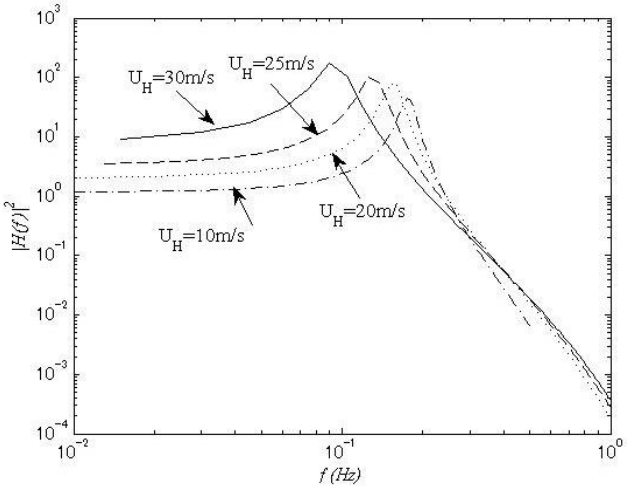


Fig. 13 Variation of mechanical admittance function with wind speed

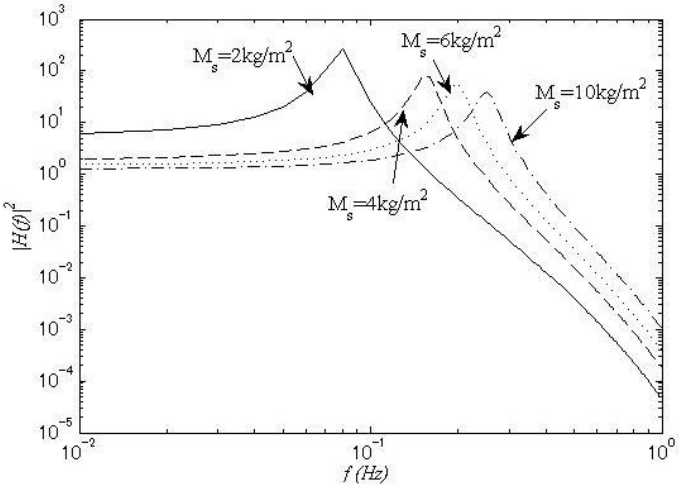


Fig. 14 Variation of mechanical admittance function with roof's mass

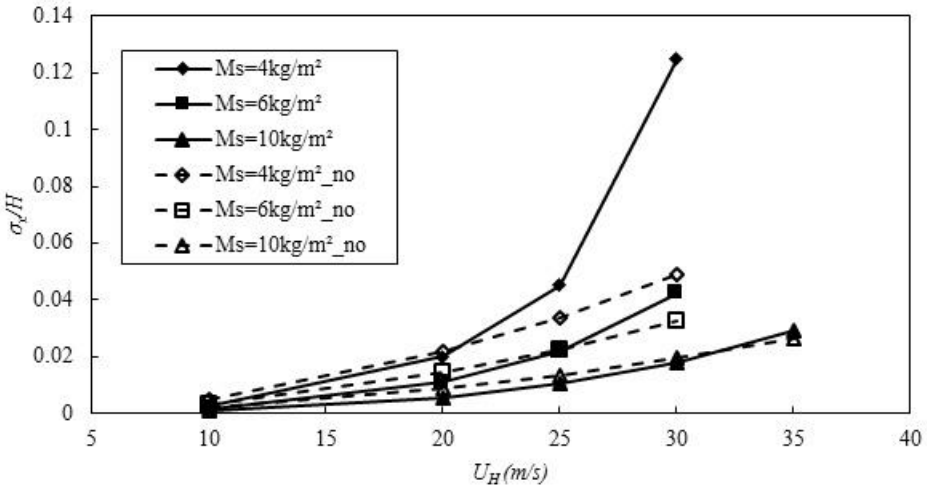


Fig. 15 Variations of standard deviation of generalized displacement ($\sigma_x$) with wind speed ($U_H$)

The relationships between $\sigma_{xj}$($j$=1) and $U_H$ were calculated for various roof's masses. Sample results are shown in Fig. 15. In the figure, the solid lines represent the results including the effect of unsteady aerodynamic forces. And the dashed lines represent the results excluding the effect of unsteady aerodynamic forces. It is found that the dynamic response becomes larger with a decrease in the roof mass. Furthermore, the unsteady aerodynamic forces will have less effect on the dynamic responses for heavier roofs, since the dynamic motion dictates the behavior. The dynamic response becomes larger with an increase in the wind speed. The response predicted by considering the effect of aerodynamic forces is larger than that predicted by neglecting the effect of unsteady aerodynamic forces, when the wind speed exceeds a certain value. In other words, the effect of unsteady aerodynamic forces on dynamic responses change from positive to negative as the wind speed increases beyond this value.

## 6. Conclusions

The unsteady aerodynamic force on a long-span curved roof has been investigated based on a wind tunnel experiment as well as on a CFD simulation. The dynamic response of a practical long-span curved roof including the influence of the unsteady aerodynamic forces has been evaluated. The main results are summarized as follow:

(1) The aerodynamic stiffness and damping coefficients vary with the reduced frequency of vibration. The coefficients are minutely influenced by the wind speed, rise/span ratio and vibration amplitude.

(2) The value of aerodynamic stiffness coefficient is generally positive, which decreases the total stiffness of system. On the other hand, the value of aerodynamic damping coefficient is negative, which may result in an increase of the total damping of system.

(3) The CFD simulation is a useful tool to evaluate the unsteady aerodynamic forces on the vibrating roof in a turbulent boundary layer. The general trends of the aerodynamic stiffness

and damping coefficients with the reduced frequency of vibration obtained from the CFD simulation are consistent with that from the wind tunnel experiment.

(4) As the roof'smass increases, the effect of the unsteady aerodynamic forces on the roof's response to turbulent winds becomes less significant. And the unsteady aerodynamic forces reduced the resonant frequency and change the resonant peak.

(5) The dynamic responses are predicted to be larger than that predicted by neglecting the effect of unsteady aerodynamic forces, when the wind speed exceeds a certain value.

## References

Cheng, C.M., Lu, P.C. and Tsai, M.S. (2002), "Acrosswind aerodynamic damping of isolated square-shaped buildings", *J. Wind Eng. Ind. Aerod.*, **90**(12-15), 1743-1756.

Chen, X.Z. (2013), "Estimation of stochastic crosswind response of wind-excited tall buildings with nonlinear aerodynamic damping", *Eng. Struct.*, **56**, 766-778.

Cooper, K.R., Nakayama, M., Sasaki, Y., Fediw, A.A., Resende-Ide, S. and Zan, S.J. (1997), "Unsteady aerodynamic force measurements on a super-tall building with a tapered cross section", *J. Wind Eng. Ind. Aerod.*, **72**(1-3), 199-212.

Daw, D.J. and Devenport, A.G. (1989), "Aerodynamic damping and stiffness of a semi-circular roof in turbulent wind", *J. Wind Eng. Ind. Aerod.*, **32**(1-2), 83-92.

Katagiri, J., Ohkuma, T. and Marukawa, H. (2001), "Motion-induced wind forces acting on rectangular high-rise buildings with side ratio of 2", *J. Wind Eng. Ind. Aerod.*, **89**(14-15), 1421-1432.

Katagiri, J., Ohkuma, T., Marukawa, H. and Tsurumi, T. (2001), "Characteristics of motion-induced wind forces during coupled across-wind and torsional vibration", *J. Struct. Constr. Eng. AIJ*, **543**, 15-22.

Lu, C.L., Li, Q.S., Huang, S.H., Chen, F.B. and Fu, X.Y. (2012), "Large eddy simulation of wind effects on a long-span complex roof structure", *J. Wind Eng. Ind. Aerod.*, **100**(1), 1-18.

Matsumoto, M., Kobayashi, Y. and Shirato, H. (1996), "The influence of aerodynamic derivatives on flutter", *J. Wind Eng. Ind. Aerod.*, **60**, 227-239.

Matsumoto, M., Matsumiya, H., Fujiwara, S. and Ito, Y. (2010), "New consideration on flutter properties based on step-by-step analysis", *J. Wind Eng. Ind. Aerod.*, **98**(8-9), 429-437.

Nozu, T. and Tamura, T. (1998), "Generation of unsteady wind data in boundary layers and its turbulence structures", *Proceedings of the 15th National symposium on wind engineering*, Tokyo, Japan, December.

Ohkuma, T. and Marukawa, H. (1990), "Mechanism of aeroelastically unstable vibration of large span roof", *J. Wind Eng.*, **42**, 35-42.

Ono, Y., Tamura, T. and Kataoka, H. (2008), "LES analysis of unsteady characteristics of conical vortex on a flat roof", *J. Wind Eng. Ind. Aerod.*, **96**(10-11), 2007-2018.

Sarwar, M.W., Ishihara, T., Shimada, K., Yamasaki, K. and Ikeda, T. (2008), "Prediction of aerodynamic characteristics of a box girder bridge section using the LES turbulence model", *J. Wind Eng. Ind. Aerod.*, **96**(10-11), 1895-1911.

Sato, H., Kusuhara, S., Ogi, K. and Matsufuji, H. (2000), "Aerodynamic characteristics of super long-span bridges with slotted box girder", *J. Wind Eng. Ind. Aerod.*, **88**(2-3), 279-306.

Uematsu, Y. and Uchiyama, K. (1982), *Wind-induced dynamic behaviour of suspended roofs*, The Technology Reports of the Tohoku University, **47**, 243-261.

Yang, Q.S., Wu, Y. and Zhu, W.L. (2010), "Experimental study on interaction between membrane structures and wind environment", *Earthq. Eng. Eng. Vib.*, **9** (4), 523-532.

## Appendix

Considering the effects of unsteady aerodynamic forces, the equation of motion for the roof in the frequency domain may be given by the following equation

$$\left(-\omega^2 M_{s_j} + i2\zeta_{s_j} M_{s_j} \omega\omega_{s_j} + \omega_{s_j}^2 M_{s_j}\right) x_j(f) = F_{W_j}(f) + \left(iF_{I_j}(f) + F_{R_j}(f)\right) \quad \text{(A.1)}$$

where $M_j$ = generalized mass; $\omega_j$ = natural circular frequency; $\zeta_j$ = critical damping ratio; $x_j$ = generalized displacement; and $F_{Wj}$ represents the fluctuating wind force due to the oncoming flow and wake instability; $F_{Rj}$ and $F_{Ij}$ are the in-phase and out-of-phase components of the unsteady aerodynamic force, respectively.

The resonant response is considered as the most important part of the wind-induced responses of long-span curved roofs. Therefore the natural frequency becomes predominant in the wind-induced responses. We transpose the unsteady aerodynamic forces to the left side of Eq. (A.1), and then obtain the aerodynamic damping ratio and aerodynamic stiffness in the case of $f = f_s$. In the Eq. (A. 2) and (A.3), $\rho_a$ is the air density and $\rho_s$ is the structural density.

$$\zeta_a(f) = -\frac{F_I}{2\omega_s^2 M_s x(f_s)} = -\frac{1}{16\pi^2}\frac{\rho_a}{\rho_s}\left(\frac{U_H}{f_s H}\right)^2 \frac{H}{L} a_C(f) \quad \text{(A.2)}$$

$$\frac{K_a}{K_s}(f) = -\frac{F_R}{\omega_s^2 M_s x(f_s)} = -\frac{1}{8\pi^2}\frac{\rho_a}{\rho_s}\left(\frac{U_H}{f_s H}\right)^2 \frac{H}{L} a_K(f) \quad \text{(A.3)}$$